Behind the dust veil: A panchromatic view of an optically dark galaxy at z = 4.82

A&A, 693, A309 (2025)
https://doi.org/10.1051/0004-6361/202452932

Astronomy & Astrophysics

Behind the dust veil: A panchromatic view of an optically dark galaxy at $z = 4.82$

Nikolaj B. Sillassen[1,2,⋆], Shuowen Jin[1,2,⋆,⋆⋆], Georgios E. Magdis[1,2,3], Jacqueline Hodge[4], Raphael Gobat[5], Emanuele Daddi[6], Kirsten Knudsen[7], Alexis Finoguenov[8], Eva Schinnerer[9], Wei-Hao Wang[10], Zhen-Kai Gao[10], John R. Weaver[11], Hiddo Algera[10,12,13], Irham T. Andika[14,15], Malte Brinch[16], Chian-Chou Chen[10], Rachel Cochrane[17,18], Andrea Enia[19,20], Andreas Faisst[21], Steven Gillman[1,2], Carlos Gomez-Guijarro[6], Ghassem Gozaliasl[8,22], Chris Hayward[23], Vasily Kokorev[24], Maya Merchant[1,3], Francesca Rizzo[25], Margherita Talia[26,20], Francesco Valentino[1,2], David Blánquez-Sesé[1,2], Anton M. Koekemoer[27], Benjamin Magnelli[6], Michael Rich[28], and Marko Shuntov[1,3]

(Affiliations can be found after the references)

Received 8 November 2024 / Accepted 12 December 2024

ABSTRACT

Optically dark dusty star-forming galaxies (DSFGs) play an essential role in massive galaxy formation at early cosmic time; however, their nature remains elusive. Here, we present a detailed case study of all the baryonic components of a $z = 4.821$ DSFG, XS55. Selected from the ultra-deep COSMOS-XS 3 GHz map with a red SCUBA-2 450 μm/850 μm colour, XS55 was followed up with ALMA 3 mm line scans and spectroscopically confirmed to be at $z = 4.821$ via detections of the CO(5-4) and [CI](1-0) lines. JWST/NIRCam imaging reveals that XS55 is a F150W drop-out with a red F277W/F444W colour and a complex morphology: a compact central component embedded in an extended structure with a likely companion. XS55 is tentatively detected in X-rays with both Chandra and XMM-Newton, suggesting an active galactic nucleus nature. By fitting a panchromatic spectral energy distribution spanning from near-infrared to radio wavelengths, we reveal that XS55 is a massive main-sequence galaxy with a stellar mass of $M_* = (5 \pm 1) \times 10^{10}\,\mathrm{M}_\odot$ and a star formation rate of $\mathrm{SFR} = 540 \pm 177\,\mathrm{M}_\odot\,\mathrm{yr}^{-1}$. The dust of XS55 is optically thick in the far-infrared with a surprisingly cold dust temperature of $T_{\mathrm{dust}} = 33 \pm 2$ K, making XS55 one of the coldest DSFGs at $z > 4$ known to date. This work unveils the nature of a radio-selected F150W drop-out, suggesting the existence of a population of DSFGs hosting active black holes embedded in optically thick dust.

Key words. galaxies: active – galaxies: general – galaxies: ISM

1. Introduction

Optically faint or dark galaxies are a population of massive dusty star-forming galaxies (DSFGs) that are faint or undetected in deep optical images, while bright at longer wavelengths. This population includes but is not limited to the following samples: sub-millimetre galaxies (SMGs) (e.g., Walter et al. 2012), *H*-band drop-outs (e.g., Wang et al. 2019; Alcalde Pampliega et al. 2019; Smail et al. 2023), Ks-faint (e.g., Smail et al. 2021), Hubble Space Telescope (HST)-dark or faint galaxies (e.g., Franco et al. 2018; Pérez-González et al. 2023; Xiao et al. 2023; Gómez-Guijarro et al. 2023), and radio-selected near-infrared (NIR) dark galaxies (Algera et al. 2020; Talia et al. 2021; Enia et al. 2022; van der Vlugt et al. 2023; Gentile et al. 2024a,b). Recent studies have revealed that this population contributes significantly (10–40%) to the cosmic star formation rate density in the early Universe ($z \sim 3$–6, Wang et al. 2019; Fudamoto et al. 2021; Talia et al. 2021; Enia et al. 2022; Shu et al. 2022; Xiao et al. 2023), and dominates the massive end of the stellar mass function at $z \sim 3$–8 (Wang et al. 2019; Gottumukkala et al. 2024). This indicates that this population plays a significant role in cosmic star formation history, even up to 50% when the contribution is estimated from Lyman break galaxy selected samples at $z \sim 3$ (Enia et al. 2022), but has been largely missed by previous optical/NIR surveys. Thanks to the unprecedented sensitivity and long wavelength coverage, the James Webb Space Telescope (JWST) can efficiently detect these objects and allows for detailed studies and a large sample census of optically faint galaxies. For example, Barrufet et al. (2023) studied the stellar emission of a sample of 30 HST-dark sources in the CEERS field with red colours through 1.6–4.4 μm in JWST/NIRCam filters, revealing them all to be heavily dust-obscured massive main-sequence galaxies that contribute significantly to the star formation rate density at high redshift. In a NIRSpec study of 23 HST-dark galaxies, Barrufet et al. (2024) found the majority to be massive ($\log(M_*/\mathrm{M}_\odot) > 9.8$) and highly attenuated ($A_V > 2$) star-forming galaxies with a broad range of recent star formation activities. Kokorev et al. (2023) studied the multi-wavelength properties of an HST-dark galaxy at $z_{\mathrm{spec}} = 2.58$ with JWST/NIRCam data, revealing it to be a massive disc galaxy with $\log(M_\star/\mathrm{M}_\odot) > 11$ and optically thick dust in the far-infrared (FIR). They also found that such objects would not be detected in JWST filters bluer than F356W if placed at $z > 4$, and becoming JWST-dark at $z > 6$ at current depths of major JWST surveys. Given their extreme faintness in optical and NIR wavelengths, and brightness in the FIR, sub-millimetre facilities like the Atacama Large Millimeter Array (ALMA) and Northern Extended Millimeter Array (NOEMA) are more efficient at confirming their redshifts via detecting CO and/or [CI] lines (e.g., Weiß et al. 2009; Walter et al. 2012; Riechers et al. 2013, 2017; Jin et al. 2019, 2022; Casey et al. 2019; Birkin et al. 2021;

⋆ Corresponding authors; nbsi@space.dtu.dk, shuji@dtu.dk
⋆⋆ Marie Curie Fellow.

Chen et al. 2022; Gentile et al. 2024b), which hence revealed vigorous star-bursting activities with obscured star formation rates, SFR $\sim$ 300−3000 $M_\odot$/yr, and large gas reservoirs, $\log M_{\rm gas}/M_\odot \sim 10.5-11.5$, in these massive systems (e.g., Riechers et al. 2013; Jin et al. 2022). However, the spectroscopic sample is still small and strongly biased towards sources with the brightest sub-millimetre fluxes. Consequently, studies of this population strongly rely on photometric redshifts, which entail the risk of catastrophic failures. For example, Ling et al. (2024) reported an optically dark photo−$z > 7$ DSFG candidate using ten bands of JWST photometry; however, it was eventually confirmed at spec−$z = 2.625$ by Jin et al. (2024) via multiple CO and [CI] line detections. Evidently, robust spectroscopic confirmation is essential to uncover the nature of these extreme dusty objects.

Despite the limited sample of spectroscopically confirmed DSFGs, recent studies have revealed optically faint or dark DSFGs have optically thick dust in FIR, massive gas reservoirs, and an elevated star formation efficiency (SFE) compared to main-sequence galaxies (Jin et al. 2019, 2022; Kokorev et al. 2023). Nevertheless, it remains unclear whether active galactic nuclei (AGNs) are present in these systems. As both X-ray and optical AGN features can be severely attenuated by dust, the AGN fraction of DSFGs could be largely underestimated (Franco et al. 2018). Therefore, panchromatic studies including deep radio observations (e.g, Delvecchio et al. 2017; Algera et al. 2020; van der Vlugt et al. 2021, 2023; Gentile et al. 2024b) are key to identify potential AGN activity in these systems. As previous studies focussed either on the stellar or interstellar medium (ISM) components, comprehensive studies of all baryonic components (stellar, dust, and gas) and AGN activity are essential to unveil their nature.

In this paper, we report the spectroscopic confirmation of the radio-selected DSFG XS55 and provide a panchromatic view of its stellar, dust, and gas components and associated AGN activity. We adopt a flat cosmology with $H_0 = 70\,{\rm km\,s^{-1}\,Mpc^{-1}}$, $\Omega_{\rm M} = 0.27$, and $\Omega_\Lambda = 0.73$, and use a Chabrier (2003) initial mass function. All magnitudes are in the AB system (Oke 1974).

2. Selection and data

2.1. Selection

XS55 was originally selected in the COSMOS-XS (Algera et al. 2020; van der Vlugt et al. 2021) catalogue with an ID = 55; hence, we dubbed it XS55. It is detected in the ultra-deep COSMOS-XS S-band image with $S_{3\,\rm GHz} = 6.35 \pm 0.96\,\mu$Jy, but undetected in the less deep COSMOS 3 GHz map (rms = 2.5 μJy, Smolčić et al. 2017), and detected in the MeerKAT image with $S_{1.3\,\rm GHz} = 10.9 \pm 2.1\,\mu$Jy (Jarvis et al. 2016; Heywood et al. 2022; Hale et al. 2024). XS55 has no optical counterpart (i.e. it is optically dark) and is not included in the COSMOS2020 catalogue (Weaver et al. 2022). It drops out in JWST F115W and F150W images, but is detected in IRAC 4.5 μm (Fig. 1) and tentatively detected (∼3σ) in the ALMA 2 mm MORA map (Casey et al. 2021). By performing the super-deblending technique (Jin et al. 2018; Liu et al. 2018) with the radio prior, we measured the deblended *Herschel* and SCUBA-2 photometry of XS55. Interestingly, it is not detected in *Herschel* images (3σ limiting depths: 250 μm = 5.3 mJy, 350 μm = 8.0 mJy, 500 μm = 8.7 mJy, Jin et al. 2018), but it is well detected in two SCUBA-2 bands, 450 μm (Gao et al. 2024) and 850 μm (Simpson et al. 2019), with a red 450 μm/850 μm colour ($S_{450\,\mu\rm m} = 5.6 \pm 1.4$ mJy, $S_{850\,\mu\rm m} = 5.7 \pm 0.8$ mJy). Assuming typical dust templates from Magdis et al. (2012), the red SCUBA-2 colour suggests a FIR photometric redshift of $z > 6$. Consequently, XS55 was followed up by two ALMA 3 mm line scan projects in Cycle 9 (ID: 2022.1.00884, PI: R. Gobat; ID: 2022.1.00863.S, PI: J. Hodge).

2.2. ALMA

The two ALMA programmes were observed for a total of 1.9 hours on source. The frequency set-ups are identical in the two programs, adopting the same set-ups as in Jin et al. (2019) and covering 84–108 GHz with three tunings. We produced measurement sets with the Common Astronomy Software Applications (CASA, McMullin et al. 2007) pipeline for each observation programme. Following the methods presented in Jin et al. (2022), Zhou et al. (2024), and Sillassen et al. (2024), the calibrated data were converted to a *uv* table format and analysed with the `GILDAS` software package in *uv* space. To enhance the signals, the *uv* tables from the two programs were combined using the task *uv_merge*. The final products reach a continuum sensitivity of 9.6 μJy/beam with a spatial resolution of 1.″6, and a line sensitivity of 12 mJy/beam over 500 km/s at ∼99 GHz. As is shown in Fig. 2 and Section 3.1, we robustly detect continuum (∼14σ) and two lines (∼10σ and ∼4σ). The dust continuum is well fitted by a point-source model using `GILDAS uvfit`, while fitting with an elliptical Gaussian does not yield useful constraints. Therefore, the dust continuum is unresolved, and we have placed an upper limit on the continuum size using Eq. (2) from Gómez-Guijarro et al. (2022) (Table 2).

2.3. JWST

XS55 was observed with JWST/NIRCam in the F115W, F150W, F277W, and F444W bands, as part of the COSMOS-Web survey (Casey et al. 2023). We used the image product versions from the Dawn JWST Archive (DJA[1], Valentino et al. 2023), and furthermore verified that these are consistent with the COSMOS-Web team's map (Shuntov et al. in prep.). XS55 is well detected in both F277W (∼10σ) and F444W (∼36σ), but not detected in both F115W and F150W (<3σ), consistent with the H drop-out selection from Wang et al. (2019).

2.4. X-ray

The COSMOS field has been fully observed in soft (0.5–2.0 keV) and hard (2.0–10 keV) X-rays with both XMM-Newton (50 ks per pointing, PI: G. Hasinger; Hasinger et al. 2007) and Chandra (∼180 ks exposure) as part of the Chandra COSMOS (C-COSMOS, PI: M. Elvis; Elvis et al. 2009) and Chandra COSMOS Legacy (PI: F. Civano; Civano et al. 2016) surveys. As is shown in Figs. 1 and 3, XS55 is tentatively detected in the soft X-ray band of Chandra with a 2.1σ significance, and detected in the stacked soft, medium, and hard X-ray XMM-Newton images with a 3.1σ significance.

3. Results

3.1. Redshift identification

After extracting the ALMA spectra in all spectral windows, we combined them into a single 1D spectrum (Fig. 2), and ran a line-searching algorithm, as in Jin et al. (2019), to search for

[1] https://dawn-cph.github.io/dja/index.html

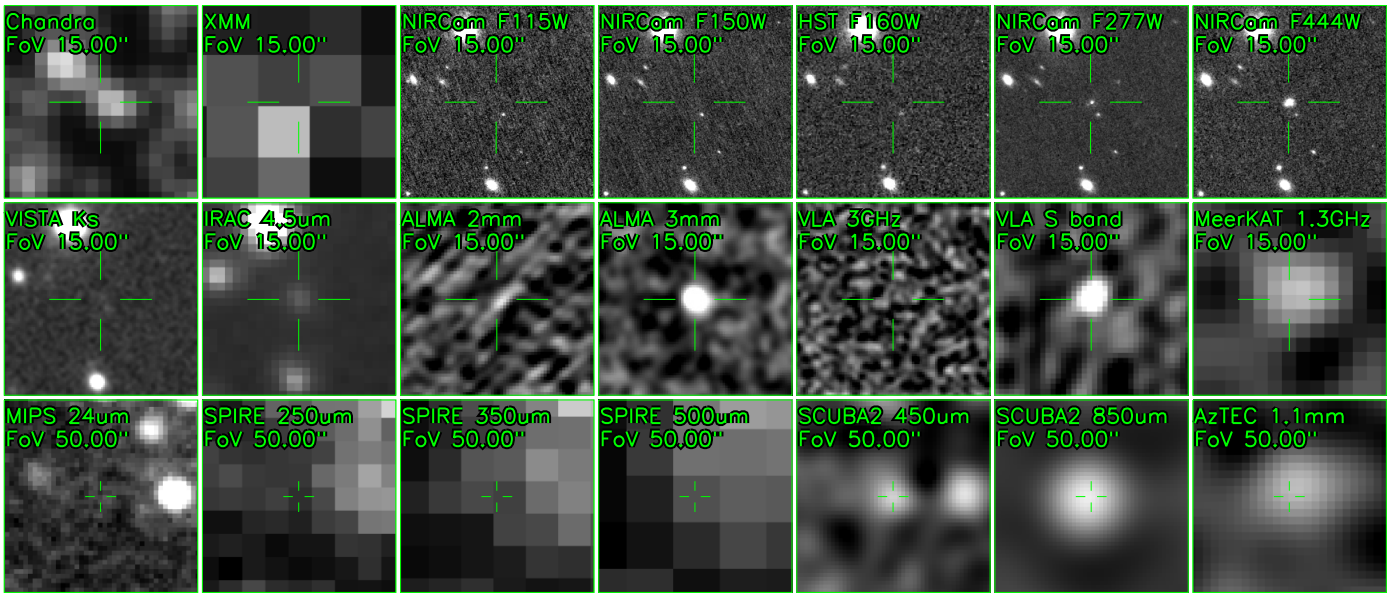

Fig. 1. Multi-wavelength cut-out images of XS55. The instrument, wavelength, and field of view are shown in green text in each panel.

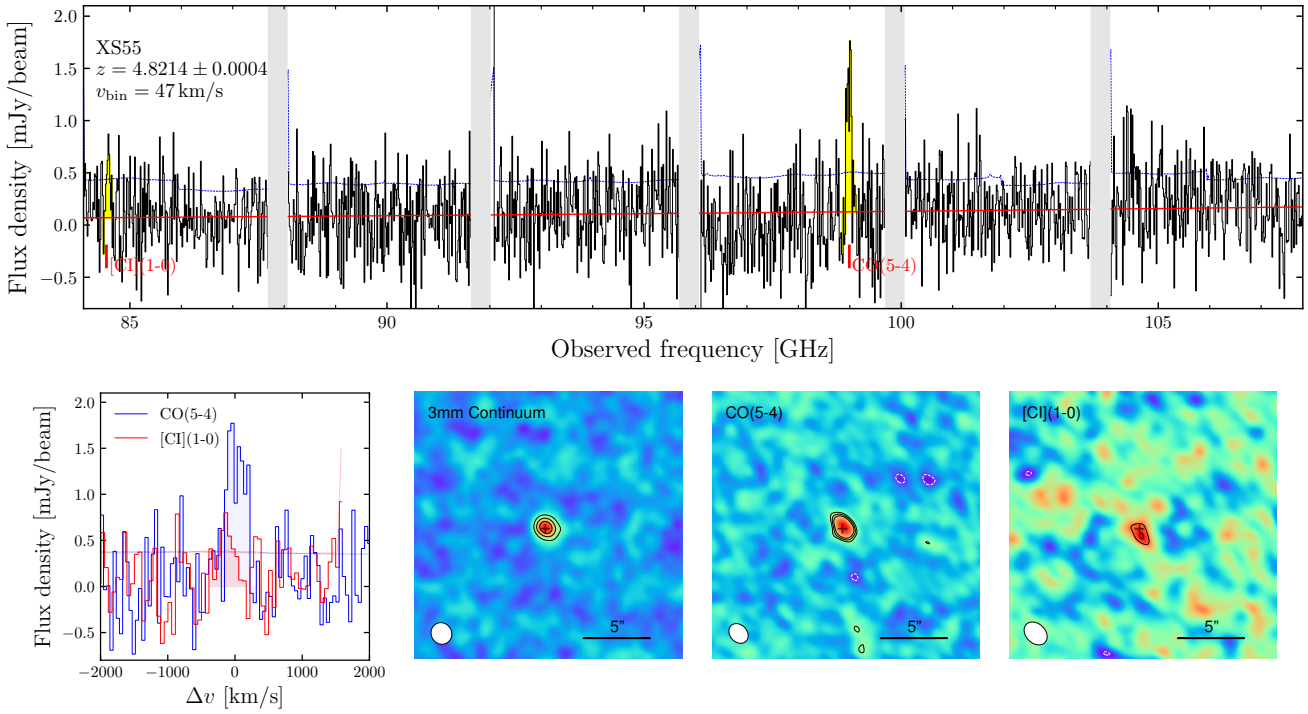

Fig. 2. ALMA 3 mm observations of XS55. *Top:* ALMA 3 mm spectrum of XS55. The red line shows the line-free continuum, and the dotted blue line indicates the flux error per channel at a 1σ level. The spectroscopic redshift is shown in text, along with the velocity width of the channels. *Bottom left:* Velocity space spectrum of CO(5-4) (blue) and [CI](1-0) (red) at $z = 4.8214$, the uncertainty per channel is shown as dashed lines. *Bottom right:* Continuum and continuum-subtracted moment-0 line maps of XS55. Contour levels are 5, 8, and 11σ for the continuum, and 3, 4, and 5σ for the line maps. The beam size is shown as a white ellipse, and the peak JWST/F444W position is marked by a grey cross.

emission line features with the highest significance. The continuum was fitted with a power law with fixed slope of 3.7 in frequency (assuming $\beta \approx 1.7$, Magdis et al. 2012; Sillassen et al. 2024), masking out the channels of significant emission lines. The detected emission lines were fitted with a Gaussian profile in the continuum subtracted spectrum. XS55 is detected in the 3 mm continuum at $\sim 14\sigma$ with a flux of $134.2 \pm 9.3\,\mu$Jy at $\sim$96 GHz. One line is detected at 98.99 GHz at 9.8σ (see Fig. 2), and we searched for other lines in the spectrum consistent with this detection. We found a 3.9σ detection at 84.58 GHz. The two lines are consistent with CO(5-4) and [CI](1-0) at $z = 4.8214 \pm 0.0004$. We note that there is a slight velocity offset between the CO and CI line peaks of $\sim$141 km/s (Fig. 2). By defining the [CI] line range using the velocity range of the CO line, the [CI] S/N is 3.3σ, yielding a low $P_{\rm chance} = 0.4\%$, where $P_{\rm chance}$ is the chance probability of finding a spurious second line

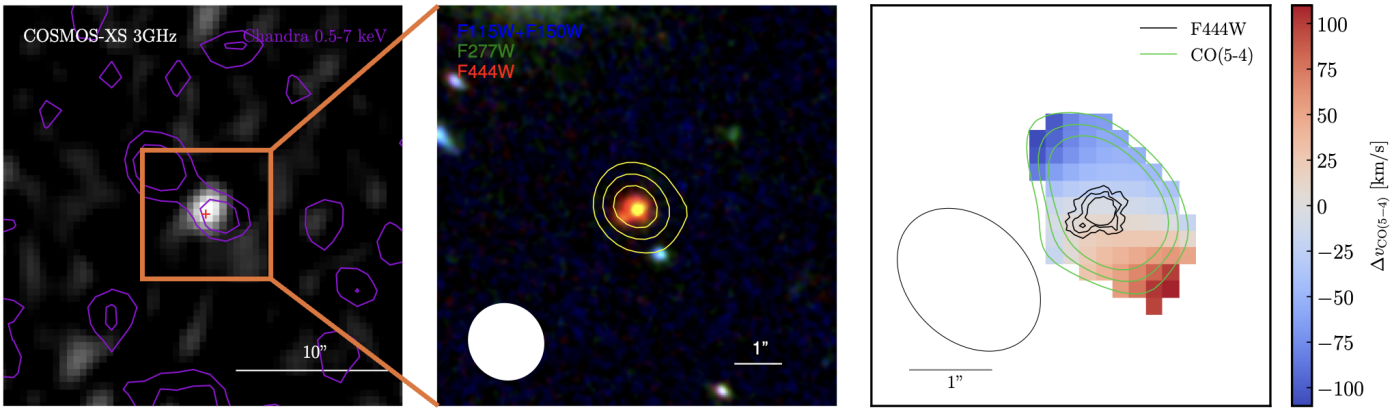

Fig. 3. Multi-wavelength images of XS55. *Left:* COSMOS-XS 3 GHz map (van der Vlugt et al. 2021) overlaid with 2, 3σ 0.5–7 keV contours from Chandra, smoothed with a 1″ Gaussian, in purple. *Middle:* JWST colour image of XS55 representing F115W+F105W, F277W, and F444W as blue, green, and red channels, respectively. Overlaid are ALMA 3 mm continuum emission contours at 5, 8, and 11σ, with the beam size shown as a white ellipse. *Right:* Moment-1 map of CO(5-4) masked at 3σ in moment-0, overlaid with integrated CO(5-4) at 3, 4, and 5σ levels and JWST/F444W contours at 5, 8, and 11σ levels in yellow and black, respectively.

Table 1. Measured properties of XS55 emission lines.

Line	S/N	FWHM [km s^{-1}]	$I_{\rm line}$ [Jy km s^{-1}]	$L'_{\rm line}$ [10^{10} K km s^{-1} pc^2]	$P_{\rm chance}$ [(a)]
CO(5-4)	9.8	365 ± 37	0.53 ± 0.07	1.9 ± 0.2	$<10^{-6}$
[CI](1-0)	3.9	293 ± 75	0.22 ± 0.06	1.1 ± 0.3	<0.004

Notes. [(a)]Chance probability of emission line (Jin et al. 2019).

(Jin et al. 2019). Further, we compared the redshift solution with the NIR spectral energy distribution (SED) fitted redshift probability distribution PDF(z) of `LePhare` in the COSMOS-Web catalogue ($z_{\rm phot} = 4.73^{+0.52}_{-0.64}$, Shuntov et al. in prep.), and found they are in excellent agreement (Fig. 4). For a sanity check, we tested the redshift solution of $z = 3.66$ in the case of the bright line being CO(4-3), as this redshift is seemingly consistent with the second peak of the NIR PDF(z). However, we found that $z = 3.66$ is very unlikely, because (1) the $z = 3.66$ [CI](1-0) is not detected at the expected frequency of 105.6 GHz (<1σ), and (2) the SED fitting at $z = 3.66$ yields an abnormally high dust-mass-to-stellar-mass fraction, $0.09 < M_{\rm dust}/M_* < 0.13$, which is >10× above typical values (e.g., Donevski et al. 2020), again disfavouring the $z = 3.66$ solution. Therefore, a multitude of evidence confirms the redshift of XS55 to be $z = 4.8214 \pm 0.0004$.

3.2. Morphology

We modelled the F277W and F444W morphology of XS55 using `Galfit` (Peng et al. 2010). We adopted three separate components in both F277W and F444W: a compact central emission, a diffuse central emission, and a companion component to the south-east. The NIRCam PSFs were obtained using Webbpsf (Perrin et al. 2014) with a pixel scale of 0.05″/pix. We considered two cases: one case using a point source (compact component) together with two Sérsic profiles (diffuse component and companion), and another case with three separate Sérsic profiles. In the case using a point source and two Sérsic models in F444W, there is a ring of emission left in the residual (Fig. A.1, middle right), suggesting that the brightest part of the galaxy is marginally resolved, or the PSF modelling is imperfect. In the case of the three Sérsic profiles, there are no clear structures, as would be expected with random noise (Fig. A.1-top). In the three-Sérsic-profile model of F444W, the compact component has a size of 0.″061 ± 0.″007, corresponding to $R_{\rm e} = 0.40 \pm 0.05$ kpc, with a Sérsic index of $n < 1.2$, while the diffuse emission and the companion have sizes and Sérsic indices of $R_{\rm e} = 1.7 \pm 0.1$ kpc, $n = 0.37 \pm 0.08$, and $R_{\rm e} = 1.1 \pm 0.1$ kpc, $n = 0.61 \pm 0.33$, respectively (Table A.1). In F444W, 33 ± 3% of the total flux is coming from the compact component, while 53 ± 3% is coming from the extended diffuse component, and 14 ± 3% is coming from the companion. In JWST/F277W, the fit of the compact component yields a bulge-like $n = 2.6 \pm 0.8$ model with $R_{\rm e} = 0.58 \pm 0.07$ kpc (Table A.1), providing 87 ± 2% of the total flux. The diffuse component cannot be fitted, and the fit to the companion yields a $n = 2.0 \pm 1.4$ model with $R_{\rm e} = 1.7 \pm 0.5$ kpc, providing 13±2% of the total flux (Section 3.2 and Table A.1). At this redshift, [OIII]$\lambda\lambda$4959, 5007 and Hβ fall within the JWST/F277W filter; consequently, the flux is possibly boosted by line emission (Fig. 4).

3.3. FIR SED

To estimate the dust mass ($M_{\rm dust}$) and temperature ($T_{\rm dust}$), we fitted the FIR and sub-millimetre photometry of XS55 with a modified black-body (MBB) model (Magdis et al. 2012) using the code `mercurius` (Witstok et al. 2022). We explored two cases: one assuming optically thin dust and another assuming 'self-consistent' optically thick dust. In the optically thick case, we placed an upper limit on the emitting area based on the half-light radius of the galaxy in JWST/F444W (9.08 kpc^2; Section 3.2). The resulting fit and corresponding parameters are shown in Fig. B.1 and Table 2. In both cases, the IR spectral index, $\beta_{\rm IR}$, is consistent with a weighted average of $\beta_{\rm IR} = 2.0 \pm 0.1$. In the optically thin case, we recovered a low dust temperature of $T_{\rm dust} = 28.0^{+3.3}_{-2.8}$ K, with an accompanying high dust mass of $M_{\rm dust} = 2.3^{+1.4}_{-0.8} \times 10^9\,{\rm M}_\odot$. On the other hand, the optically thick dust yields a higher $T_{\rm dust} = 32.7^{+2.2}_{-1.9}$ K and a lower $M_{\rm dust} = 1.7^{+0.6}_{-0.5} \times 10^9\,{\rm M}_\odot$.

To construct a panchromatic SED of XS55, we fitted the stellar, AGN, and dust components using `STARDUST` (Kokorev et al. 2021) and available photometry from optical to radio wavelengths, yielding an IR luminosity of $L_{\rm IR} = (5.4 \pm 1.8) \times 10^{12}\,{\rm L}_\odot$ and ${\rm SFR}_{\rm IR} = 540 \pm 180\,{\rm M}_\odot\,{\rm yr}^{-1}$. For the stellar component,

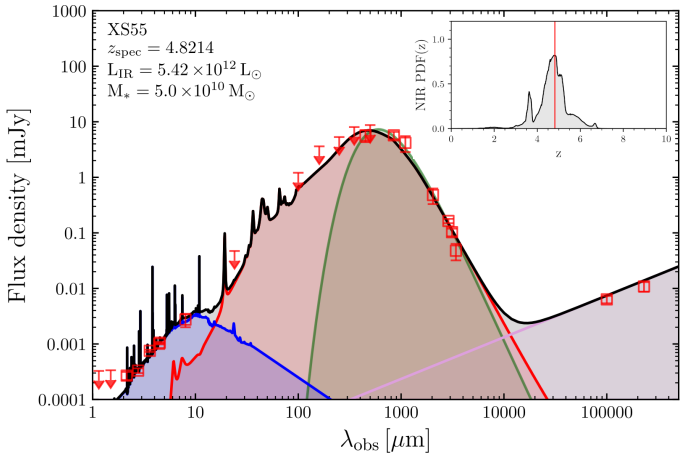

Fig. 4. NIR to radio SED of XS55, fitted using `STARDUST` (Kokorev et al. 2021). The total SED (black) is shown with its different components: stellar (blue), dust (red), and radio (magenta). An optically thick MBB (Magdis et al. 2012), fitted with `mercurius` (Witstok et al. 2022), is shown with a green line. The MBB is not accounted for in the total SED fit. The radio component was extrapolated using the stellar-mass-dependent IR-radio relation from Delvecchio et al. (2021). The NIR PDF(z) of XS55 is shown as an inset with the spec-z marked by a vertical red line.

we recovered the stellar mass $\log(M_*/M_\odot) = 10.7 \pm 0.1$, attenuated by $A_v = 2.2 \pm 0.3$ mag. As an additional check, we also fitted the stellar part of the spectrum (up to F444W) using `Bagpipes`[2] (Carnall et al. 2018), using the same parameters as in Jin et al. (2024), yielding physical properties similar to those from `STARDUST`, $\log(M_{*,\rm bagpipes}/M_\odot) = 10.7 \pm 0.1$, $A_{\rm v,bagpipes} = 2.1 \pm 0.3$. The physical parameters calculated with LePhare in the COSMOS-Web catalogue (Shuntov et al. in prep.) also agree with our results ($\log(M_{*,\rm LePhare}/M_\odot) = 10.8 \pm 0.3$, $E(B-V)_{\rm LePhare} = 1.1$). The resulting panchromatic SED and corresponding properties from `STARDUST`, and the MBB fit from `mercurius`, are shown in Fig. 4 and Table 2.

3.4. Molecular gas mass and far-infrared lines

With the derived dust mass, we inferred a molecular gas mass ($M_{\rm mol}$) using the standard gas-to-dust mass ratio of star-forming galaxies ($\delta_{\rm gdr} = 100$, assuming solar metallicity, Magdis et al. 2012), yielding $M_{\rm mol,thin} = 2.6^{+0.5}_{-0.4} \times 10^{11}\,M_\odot$ and $M_{\rm mol,thick} = 1.7^{+0.5}_{-0.4} \times 10^{11}\,M_\odot$. Furthermore, based on the detection of the [CI](1-0) line (Table 1), we inferred the molecular gas mass, $M_{\rm mol}/\alpha_{\rm CI} = (1.8 \pm 0.5) \times 10^{11}/\alpha_{\rm CI}\,M_\odot$, where $\alpha_{\rm CI} = 17.0 \pm 0.3\,M_\odot\,K^{-1}\,km^{-1}\,s\,pc^{-2}$ (Dunne et al. 2022), which is consistent with other calibrations (Valentino et al. 2018; Heintz & Watson 2020). Adopting instead $\alpha_{\rm CI} = 4.1 \pm 1.4\,M_\odot\,K^{-1}\,km^{-1}\,s\,pc^{-2}$ from Frias Castillo et al. (2024) for high-z SMGs yields $M_{\rm mol} = (4.3 \pm 1.9) \times 10^{10}\,M_\odot$. Interestingly, the CO(5-4) emission is marginally resolved in the north-east to south-west direction (see Figs. 2 and 3), as the minor axis of the CO emission as well as the continuum source are unresolved, and we obtained upper limits on their sizes using Eq. (2) of Gómez-Guijarro et al. (2022). We measured the size of the integrated CO(5-4) emission by fitting an elliptical Gaussian in uv space with `GILDAS/uvfit`, and obtained $R_e = 1.79 \pm 1.22$ kpc with PA $= 28 \pm 20$ deg. We constructed the CO(5-4) moment-1 map using the Cube Analysis and Rendering Tool for Astronomy (`CARTA`; Comrie et al. 2021, Fig. 3-right). In the moment-1 map, there is a clear velocity gradient, with the highest redshifted velocity being 70 km/s and the highest blueshifted velocity being −130 km/s. This velocity gradient is comparable to that of the radio selected NIR-dark galaxies from Gentile et al. (2024b). We discuss the possible interpretations of the extended CO(5-4) emission in Sect. 4.2.

[2] https://bagpipes.readthedocs.io/en/latest/

Table 2. Fitted and inferred physical properties of XS55.

Parameter	Value
ID	XS55
RA, Dec [deg]	150.1002501, 2.4967382
z	4.8214 ± 0.0004
A_V [mag]	2.2 ± 0.3
M_* [$10^{10}\,M_\odot$]	5 ± 1
$\rm SFR_{IR}$ [$M_\odot\,yr^{-1}$]	540 ± 180
$L_{\rm X}$ [10^{44} erg s^{-1}]	>5.4
$L_{\rm IR}$ [$10^{12}\,L_\odot$]	5.4 ± 1.8
$\beta_{\rm IR}$	2.0 ± 0.2
$M_{\rm gas,[CI]}$ [$10^{11}\,M_\odot$]	1.8 ± 0.5
SFE [10^{-9} yr^{-1}]	3.0 ± 1.0
$T_{\rm dust,thick}$ [K]	$32.7^{+2.2}_{-1.9}$
$M_{\rm dust,thick}$ [$10^9\,M_\odot$]	$1.7^{+0.6}_{-0.5}$
$T_{\rm dust,thin}$ [K]	$28.0^{+3.3}_{-2.8}$
$M_{\rm dust,thin}$ [$10^9\,M_\odot$]	$2.3^{+1.4}_{-0.8}$
$R_{\rm eff,3\,mm}$ [kpc]	<1.76 (*)
$R_{\rm maj,CO(5-4)}$ [kpc]	3.2 ± 1.1
$R_{\rm min,CO(5-4)}$ [kpc]	<2.08 (*)
$\rm PA_{CO(5-4)}$ [deg]	28 ± 20

Notes. (*)Size upper limit (2σ) calculated with Eq. (2) in Gómez-Guijarro et al. (2022).

3.5. Obscured active galactic nucleus

XS55 is tentatively detected in X-ray with both Chandra and XMM-Newton (Figs. 3, 1). Using a 3″ radius aperture that corresponds to the mean PSF of the Chandra COSMOS Legacy Survey (Civano et al. 2016), we detected three counts in the 0.5–2 keV band of Chandra. This corresponds to a flux of $f_{[0.5-2\,\rm keV]} = (1.15 \pm 0.54) \times 10^{-16}$ erg s^{-1} cm^{-2} adopting the conversion rate from Civano et al. (2016). Since XS55 is extremely dusty, this flux should be considered a lower limit, yielding a soft X-ray luminosity of $L_{[0.5-2\,\rm keV]} > 2.81 \times 10^{43}$ erg s^{-1}. Using the soft X-ray to bolometric luminosity correction from Lusso et al. (2012), we obtained a bolometric luminosity of $L_{\rm bol} > 5.35 \times 10^{44}$ erg s^{-1}. XS55 would be an X-ray selected AGN using the criterion from Riccio et al. (2023) (i.e. $L_{0.2-2.3\rm keV} \geq 3 \times 10^{42}$ erg s^{-1}). Due to the low significance of the X-ray detection, we cannot exclude that the detection could be spurious, or is originating from star formation. XS55 does not show excess radio emission compared to the infrared radio correlation of Delvecchio et al. (2021); however, this could be due to the large scatter of IR-radio correlation that is largely unconstrained at $z \sim 5$ (Delvecchio et al. 2021). Furthermore, while radio excess is a clear indicator of AGN activity, X-ray AGNs are not necessarily radio-loud.

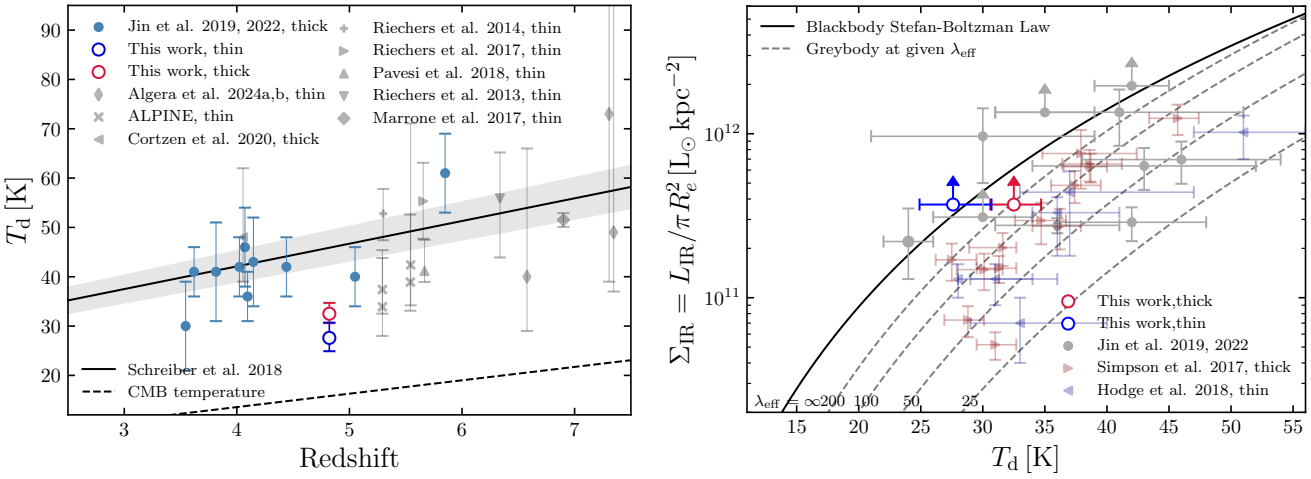

Fig. 5. Dust properties of XS55. *Left:* Dust temperature vs. redshift for XS55 and literature samples. The $T_d - z$ relation of main-sequence galaxies from Schreiber et al. (2018) is shown as a black line, with the uncertainty as the shaded grey area. The literature samples are from Riechers et al. (2013, 2014, 2017), Marrone et al. (2018), Pavesi et al. (2018), Faisst et al. (2020), Jin et al. (2019, 2022), Fudamoto et al. (2023), and Algera et al. (2024a,b). The CMB temperature as a function of redshift is shown as a dashed black line. *Right:* Infrared luminosity surface density as a function of dust temperature, assuming optically thick dust. The surface density limit as defined by the Stefan-Boltzman law of optically thin dust is shown as a black line, while grey-bodies with varying λ_{eff} are shown as dashed lines. The literature samples are from Simpson et al. (2017), Hodge et al. (2019), and Jin et al. (2019, 2022).

4. Discussion

4.1. Intrinsically cold or optically thick dust

To determine whether XS55 is intrinsically cold, or optically thick dust is making it appear cold, we applied three methods of diagnosing optically thick dust from Jin et al. (2022): (1) We compared the molecular gas masses derived from [CI](1-0) emission with gas mass inferred by both thin and thick M_{dust}. We find that the lower gas mass from the thick dust model is in good agreement with the [CI]-derived gas mass, assuming $\delta_{gdr} = 100$ and $\alpha_{[CI]} = 17 \pm 3\,M_\odot\,K^{-1}\,km^{-1}\,s\,pc^{-2}$, while the gas mass from the thin dust model is likely overestimated. (2) We estimated the dust opacity at 100 µm, $\tau_{100\,\mu m} = \kappa\rho R_e$, where κ is adopted from Jones et al. (2013), and ρ is the volumetric dust density assuming spherical symmetry, using R_e from dust continuum ($R_e < 1.76$ kpc). This yields $\tau_{100\,\mu m,thin} > 1.6$, and $\tau_{100\,\mu m,thick} > 1.2$. Furthermore, we calculated the surface SFR density and find $\Sigma_{SFR} > 37\,M_\odot\,yr^{-1}\,kpc^{-2}$. With both $\tau_{100\,\mu m} > 1$ and $\Sigma_{SFR} > 20\,M_\odot\,yr^{-1}\,kpc^{-2}$, the dust is hence optically thick (Jin et al. 2022). (3) We derived a lower limit for the IR luminosity surface density, $\Sigma_{IR} > 3.7 \times 10^{11}\,L_\odot\,kpc^{-2}$, and placed it on the $\Sigma_{IR} - T_{dust}$ diagram. As is seen in Fig. 5-right, the thin case is clearly violating the black-body Stefan-Boltzmann law, and the optically thick case is more favourable. Therefore, these pieces of evidence together imply that the dust of XS55 is optically thick in the FIR.

Interestingly, the recovered T_{dust} assuming optically thick dust remains cold. Compared to the redshift evolution of T_{dust} in main-sequence galaxies (Schreiber et al. 2018; Jin et al. 2022), the thick dust solution is 0.13 dex ($\sim 4\sigma$) below the relation (Fig. 5). This makes XS55 one of the coldest DSFGs at $z > 4$ discovered to date (e.g., Faisst et al. 2020; Jin et al. 2022; Algera et al. 2024a). Since the dust temperature is proportional to the radiation field (i.e., $\langle U \rangle = (T_d/18.9)^{6.04}$, Magdis et al. 2012), and the radiation field is proportional to the ratio of SFE to metallicity (i.e., $\langle U \rangle \propto$ SFE/Z, Magdis et al. 2012), and given that XS55 has typical SFE of DSFGs, the intrinsically low dust temperature could suggest a high metallicity in XS55, where the cooling is more efficient.

4.2. Origin of extended CO(5-4)

Interestingly, the CO(5-4) is more extended than the dust continuum size and shows a tentative velocity gradient. These properties could suggest a rotating molecular disc (e.g., Rizzo et al. 2023) with compact star formation (e.g., Cochrane et al. 2019). However, given the low spatial resolution of the CO data, high-resolution data are needed to confirm whether it is a rotating disc (e.g., Rowland et al. 2024). As is suggested by the complex JWST morphology, a galaxy interaction or merger can also account for the extended CO(5-4) emission. Furthermore, given the possible AGN nature of XS55 and that the CO(5-4) is only resolved in one direction, a molecular outflow driven by a central AGN (e.g., Lutz et al. 2020) is also a potential scenario. To disentangle the above scenarios, a high-resolution [CII] follow-up would be ideal to reveal the kinematics of XS55.

4.3. Why this source is optically faint

In nearly all terms, XS55 is a normal but massive main-sequence star-forming galaxy at $z = 4.8214$, within 2σ of the Schreiber et al. (2015) main-sequence relation (ΔMS(SFR/SFR$_{MS}$) = 2.4 ± 0.9). Its SFE, and thereby its depletion time of 300 ± 100 Myr, is comparable to other optically faint galaxies at similar redshift (e.g., Jin et al. 2019, 2022). However, with the compact stellar ($R_e = 1.72 \pm 0.13$ kpc) and dust continuum ($R_e < 1.76$ kpc) sizes, XS55 falls 2.6× below the mass-size relation of main-sequence galaxies (Ward et al. 2024). The compact size, together with a massive amount of dust, could explain the optically faint nature of this source, in agreement with observations from Gómez-Guijarro et al. (2023) and simulations from Cochrane et al. (2024).

5. Conclusions

By combining ALMA spectroscopy with JWST imaging and multi-wavelength ancillary data in the COSMOS field, we have presented a detailed study of a newly discovered, radio-selected, optically faint galaxy, XS55. ALMA detections of the CO(5-4) and [CI](1-0) lines places the source at $z = 4.8214$, and reveals the presence of large amounts of dust in the ISM ($M_{\rm dust} = (1.7 \pm 0.5) \times 10^9\,{\rm M}_\odot$). XS55 is a compact massive main-sequence galaxy with an extremely cold dust temperature and optically thick FIR emission. The F444W size of the source falls below the mass-size relation. The tentative X-ray emission and the compactness of the central component suggest the presence of an AGN. The compactness together with the massive amount of cold dust in XS55 naturally explain its optical faintness.

Acknowledgements. We thank the anonymous referee for constructive comments, improving this manuscript. This paper makes use of the following ALMA data: ADS/JAO.ALMA#2022.1.00884.S, 2022.1.00863.S and 2021.1.00225.S. ALMA is a partnership of ESO (representing its member states), NSF (USA) and NINS (Japan), together with NRC (Canada), MOST and ASIAA (Taiwan), and KASI (Republic of Korea), in cooperation with the Republic of Chile. The Joint ALMA Observatory is operated by ESO, AUI/NRAO and NAOJ. Some of the data products presented herein were retrieved from the Dawn JWST Archive (DJA). DJA is an initiative of the Cosmic Dawn Center (DAWN). The Cosmic Dawn Center (DAWN) is funded by the Danish National Research Foundation under grant DNRF140. SJ acknowledges financial support from the European Union's Horizon Europe research and innovation program under the Marie Skłodowska-Curie grant No. 101060888. GEM and SJ acknowledge the Villum Fonden research grants 37440 and 13160. JH acknowledges support from the ERC Consolidator Grant 101088676 ("VOYAJ"). CCC acknowledges the support of the Taiwan National Science and Technology Council (111-2112M-001-045-MY3), as well as the Academia Sinica through the Career Development Award (AS-CDA-112-M02). KK acknowledges support from the Knut and Alice Wallenberg Foundation (KAW 2017.0292 and 2019.0443).

References

Alcalde Pampliega, B., Pérez-González, P. G., Barro, G., et al. 2019, ApJ, 876, 135
Algera, H. S. B., van der Vlugt, D., Hodge, J. A., et al. 2020, ApJ, 903, 139
Algera, H. S. B., Inami, H., De Looze, I., et al. 2024a, MNRAS, 533, 3098
Algera, H. S. B., Inami, H., Sommovigo, L., et al. 2024b, MNRAS, 527, 6867
Barrufet, L., Oesch, P. A., Weibel, A., et al. 2023, MNRAS, 522, 449
Barrufet, L., Oesch, P., Marques-Chaves, R., et al. 2024, arXiv e-prints [arXiv:2404.08052]
Birkin, J. E., Weiss, A., Wardlow, J. L., et al. 2021, MNRAS, 501, 3926
Carnall, A. C., McLure, R. J., Dunlop, J. S., & Davé, R. 2018, MNRAS, 480, 4379
Casey, C. M., Zavala, J. A., Aravena, M., et al. 2019, ApJ, 887, 55
Casey, C. M., Zavala, J. A., Manning, S. M., et al. 2021, ApJ, 923, 215
Casey, C. M., Kartaltepe, J. S., Drakos, N. E., et al. 2023, ApJ, 954, 31
Chabrier, G. 2003, PASP, 115, 763
Chen, C.-C., Liao, C.-L., Smail, I., et al. 2022, ApJ, 929, 159
Civano, F., Marchesi, S., Comastri, A., et al. 2016, ApJ, 819, 62
Cochrane, R. K., Hayward, C. C., Anglés-Alcázar, D., et al. 2019, MNRAS, 488, 1779
Cochrane, R. K., Anglés-Alcázar, D., Cullen, F., & Hayward, C. C. 2024, ApJ, 961, 37
Comrie, A., Wang, K.-S., Hsu, S.-C., et al. 2021, https://doi.org/10.5281/zenodo.4905459
Delvecchio, I., Smolčić, V., Zamorani, G., et al. 2017, A&A, 602, A3
Delvecchio, I., Daddi, E., Sargent, M. T., et al. 2021, A&A, 647, A123
Donevski, D., Lapi, A., Małek, K., et al. 2020, A&A, 644, A144
Dunne, L., Maddox, S. J., Papadopoulos, P. P., Ivison, R. J., & Gomez, H. L. 2022, MNRAS, 517, 962
Elvis, M., Civano, F., Vignali, C., et al. 2009, ApJS, 184, 158
Enia, A., Talia, M., Pozzi, F., et al. 2022, ApJ, 927, 204
Faisst, A. L., Fudamoto, Y., Oesch, P. A., et al. 2020, MNRAS, 498, 4192
Franco, M., Elbaz, D., Béthermin, M., et al. 2018, A&A, 620, A152
Frias Castillo, M., Rybak, M., Hodge, J. A., et al. 2024, arXiv e-prints [arXiv:2404.05596]
Fudamoto, Y., Oesch, P. A., Schouws, S., et al. 2021, Nature, 597, 489
Fudamoto, Y., Inoue, A. K., & Sugahara, Y. 2023, MNRAS, 521, 2962
Gao, Z.-K., Lim, C.-F., Wang, W.-H., et al. 2024, ApJ, 971, 117
Gentile, F., Talia, M., Behiri, M., et al. 2024a, ApJ, 962, 26
Gentile, F., Talia, M., Daddi, E., et al. 2024b, A&A, 687, A288
Gómez-Guijarro, C., Elbaz, D., Xiao, M., et al. 2022, A&A, 658, A43
Gómez-Guijarro, C., Magnelli, B., Elbaz, D., et al. 2023, A&A, 677, A34
Gottumukkala, R., Barrufet, L., Oesch, P. A., et al. 2024, MNRAS, 530, 966
Hale, C. L., Heywood, I., Jarvis, M. J., et al. 2024, MNRAS, 536, 2187
Hasinger, G., Cappelluti, N., Brunner, H., et al. 2007, ApJS, 172, 29
Heintz, K. E., & Watson, D. 2020, ApJ, 889, L7
Heywood, I., Jarvis, M. J., Hale, C. L., et al. 2022, MNRAS, 509, 2150
Hodge, J. A., Smail, I., Walter, F., et al. 2019, ApJ, 876, 130
Jarvis, M., Taylor, R., Agudo, I., et al. 2016, in MeerKAT Science: On the Pathway to the SKA, 6
Jin, S., Daddi, E., Liu, D., et al. 2018, ApJ, 864, 56
Jin, S., Daddi, E., Magdis, G. E., et al. 2019, ApJ, 887, 144
Jin, S., Daddi, E., Magdis, G. E., et al. 2022, A&A, 665, A3
Jin, S., Sillassen, N. B., Hodge, J., et al. 2024, A&A, 690, L16
Jones, A. P., Fanciullo, L., Köhler, M., et al. 2013, A&A, 558, A62
Kokorev, V. I., Magdis, G. E., Davidzon, I., et al. 2021, ApJ, 921, 40
Kokorev, V., Jin, S., Magdis, G. E., et al. 2023, ApJ, 945, L25
Ling, C., Sun, B., Cheng, C., et al. 2024, ApJ, 969, L28
Liu, D., Daddi, E., Dickinson, M., et al. 2018, ApJ, 853, 172
Lusso, E., Comastri, A., Simmons, B. D., et al. 2012, MNRAS, 425, 623
Lutz, D., Sturm, E., Janssen, A., et al. 2020, A&A, 633, A134
Magdis, G. E., Daddi, E., Béthermin, M., et al. 2012, ApJ, 760, 6
Marrone, D. P., Spilker, J. S., Hayward, C. C., et al. 2018, Nature, 553, 51
McMullin, J. P., Waters, B., Schiebel, D., Young, W., & Golap, K. 2007, in Astronomical Data Analysis Software and Systems XVI, eds. R. A. Shaw, F. Hill, & D. J. Bell, Astronomical Society of the Pacific Conference Series, 376, 127
Oke, J. B. 1974, ApJS, 27, 21
Pavesi, R., Riechers, D. A., Sharon, C. E., et al. 2018, ApJ, 861, 43
Peng, C. Y., Ho, L. C., Impey, C. D., & Rix, H.-W. 2010, AJ, 139, 2097
Pérez-González, P. G., Barro, G., Annunziatella, M., et al. 2023, ApJ, 946, L16
Perrin, M. D., Sivaramakrishnan, A., Lajoie, C.-P., et al. 2014, in Space Telescopes and Instrumentation 2014: Optical, Infrared, and Millimeter Wave, eds. J. M. Oschmann, Jr. M. Clampin, G. G. Fazio, & H. A. MacEwen, Society of Photo-Optical Instrumentation Engineers (SPIE) Conference Series, 9143, 91433X
Riccio, G., Yang, G., Małek, K., et al. 2023, A&A, 678, A164
Riechers, D. A., Bradford, C. M., Clements, D. L., et al. 2013, Nature, 496, 329
Riechers, D. A., Carilli, C. L., Capak, P. L., et al. 2014, ApJ, 796, 84
Riechers, D. A., Leung, T. K. D., Ivison, R. J., et al. 2017, ApJ, 850, 1
Rizzo, F., Roman-Oliveira, F., Fraternali, F., et al. 2023, A&A, 679, A129
Rowland, L. E., Hodge, J., Bouwens, R., et al. 2024, MNRAS, 535, 2068
Schreiber, C., Pannella, M., Elbaz, D., et al. 2015, A&A, 575, A74
Schreiber, C., Elbaz, D., Pannella, M., et al. 2018, A&A, 609, A30
Shu, X., Yang, L., Liu, D., et al. 2022, ApJ, 926, 155
Sillassen, N. B., Jin, S., Magdis, G. E., et al. 2024, A&A, 690, A55
Simpson, J. M., Smail, I., Swinbank, A. M., et al. 2017, ApJ, 839, 58
Simpson, J. M., Smail, I., Swinbank, A. M., et al. 2019, ApJ, 880, 43
Smail, I., Dudzevičiūtė, U., Stach, S. M., et al. 2021, MNRAS, 502, 3426
Smail, I., Dudzevičiūtė, U., Gurwell, M., et al. 2023, ApJ, 958, 36
Smolčić, V., Novak, M., Bondi, M., et al. 2017, A&A, 602, A1
Talia, M., Cimatti, A., Giulietti, M., et al. 2021, ApJ, 909, 23
Valentino, F., Magdis, G. E., Daddi, E., et al. 2018, ApJ, 869, 27
Valentino, F., Brammer, G., Gould, K. M. L., et al. 2023, ApJ, 947, 20
van der Vlugt, D., Algera, H. S. B., Hodge, J. A., et al. 2021, ApJ, 907, 5
van der Vlugt, D., Hodge, J. A., Jin, S., et al. 2023, ApJ, 951, 131
Walter, F., Decarli, R., Carilli, C., et al. 2012, Nature, 486, 233
Wang, T., Schreiber, C., Elbaz, D., et al. 2019, Nature, 572, 211
Ward, E., de la Vega, A., Mobasher, B., et al. 2024, ApJ, 962, 176
Weaver, J. R., Kauffmann, O. B., Ilbert, O., et al. 2022, ApJS, 258, 11
Weiß, A., Ivison, R. J., Downes, D., et al. 2009, ApJ, 705, L45
Witstok, J., Smit, R., Maiolino, R., et al. 2022, MNRAS, 515, 1751
Xiao, M. Y., Elbaz, D., Gómez-Guijarro, C., et al. 2023, A&A, 672, A18
Zhou, L., Wang, T., Daddi, E., et al. 2024, A&A, 684, A196

[1] Cosmic Dawn Center (DAWN), Copenhagen, Denmark
[2] DTU-Space, Technical University of Denmark, Elektrovej 327, DK-2800 Kgs. Lyngby, Denmark
[3] Niels Bohr Institute, University of Copenhagen, Jagtvej 128, DK-2200 Copenhagen, Denmark

[4] Leiden Observatory, Leiden University, NL-2300 RA Leiden, The Netherlands
[5] Instituto de Física, Pontificia Universidad Católica de Valparaíso, Casilla 4059, Valparaíso, Chile
[6] Université Paris-Saclay, Université Paris Cité, CEA, CNRS, AIM, Paris, France
[7] Department of Space, Earth, & Environment, Chalmers University of Technology, Chalmersplatsen 4, 412 96 Gothenburg, Sweden
[8] Department of Physics, University of Helsinki, PO Box 64, 00014 Helsinki, Finland
[9] Max-Planck-Institut für Astronomie, Königstuhl 17, D-69117 Heidelberg, Germany
[10] Academia Sinica Institute of Astronomy and Astrophysics (ASIAA), No. 1, Section 4, Roosevelt Rd., Taipei 106216, Taiwan
[11] Department of Astronomy, University of Massachusetts, Amherst, MA 01003, USA
[12] Hiroshima Astrophysical Science Center, Hiroshima University, 1-3-1 Kagamiyama, Higashi-Hiroshima, Hiroshima 739-8526, Japan
[13] National Astronomical Observatory of Japan, 2-21-1, Osawa, Mitaka, Tokyo, Japan
[14] Technical University of Munich, TUM School of Natural Sciences, Department of Physics, James-Franck-Str. 1, D-85748 Garching, Germany
[15] Max-Planck-Institut für Astrophysik, Karl-Schwarzschild-Str. 1, D85748 Garching, Germany
[16] Instituto de Física y Astronomía, Universidad de Valparaíso, Avda. Gran Bretana 1111, Valparaíso, Chile
[17] Institute for Astronomy, University of Edinburgh, Royal Observatory, Blackford Hill, Edinburgh EH9 3HJ, UK
[18] Department of Astronomy, Columbia University, New York, NY 10027, USA
[19] University of Bologna– Department of Physics and Astronomy "Augusto Righi" (DIFA), Via Gobetti 93/2, I-40129 Bologna, Italy
[20] INAF–Osservatorio di Astrofisica e Scienza dello Spazio, Via Gobetti 93/3, I-40129 Bologna, Italy
[21] Caltech/IPAC, 1200 E. California Boulevard, Pasadena, CA 91125, USA
[22] Department of Computer Science, Aalto University, PO Box 15400, Espoo 00 076, Finland
[23] Center for Computational Astrophysics, Flatiron Institute, 162 Fifth Avenue, New York, NY 10010, USA
[24] Department of Astronomy, The University of Texas at Austin, Austin, TX 78712, USA
[25] Kapteyn Astronomical Institute, University of Groningen, Landleven 12, 9747 AD Groningen, The Netherlands
[26] University of Bologna, Department of Physics and Astronomy (DIFA), Via Gobetti 93/2, I-40129 Bologna, Italy
[27] Space Telescope Science Institute, 3700 San Martin Drive, Baltimore, MD 21218, USA
[28] Department of Physics & Astronomy, University of California Los Angeles, 430 Portola Plaza, Los Angeles, CA 90095, USA

Appendix A: Morphology

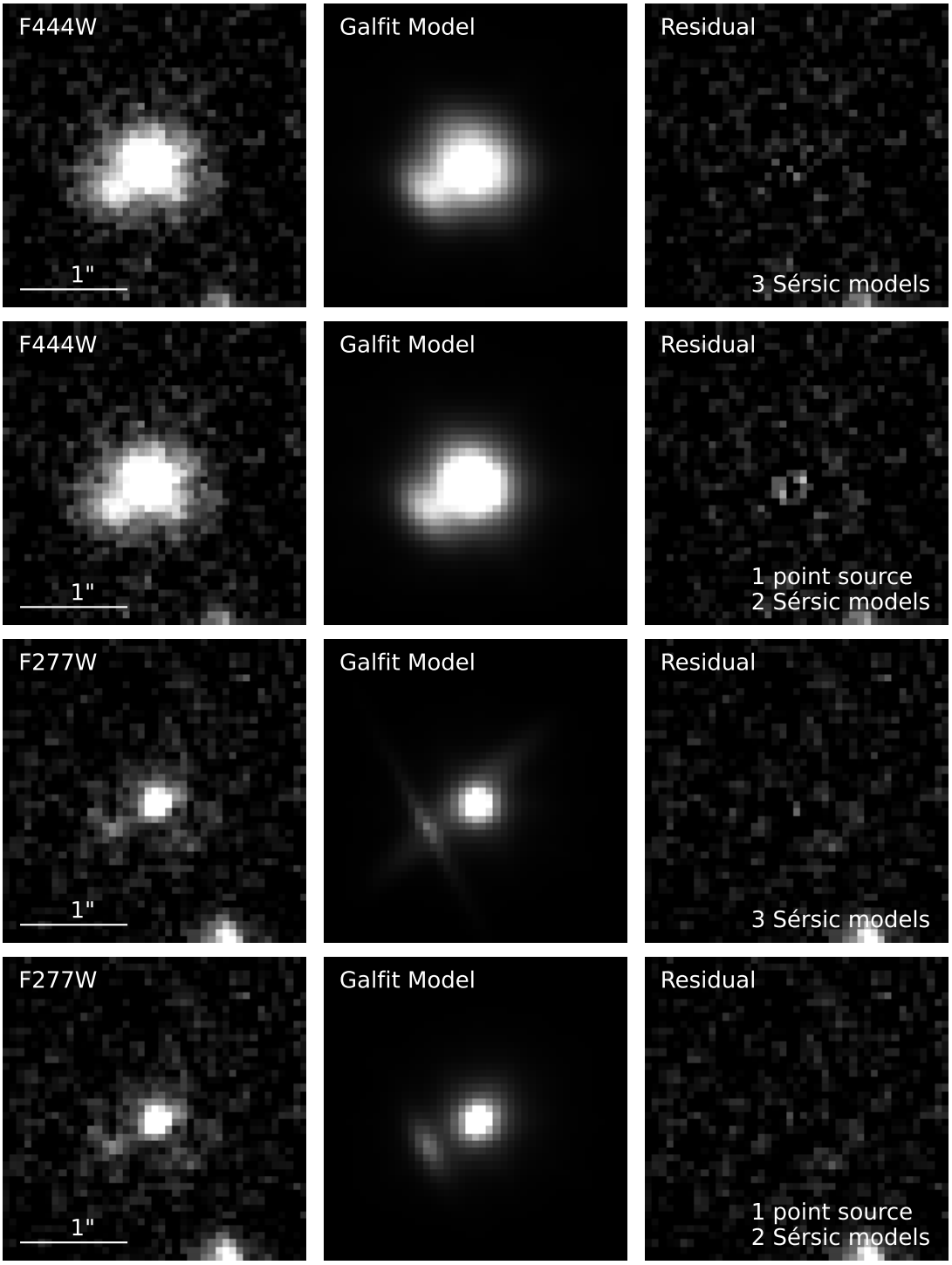

Fig. A.1. Morphological fit of XS55 in JWST/F444W (top and middle row) and JWST/F277W (bottom row). The different components of each fit are stated in the right column of each row.

Table A.1. Effective radii and Sérsic indices from Galfit

F444W	
Compact component	
$R_{e,F444W}$ [kpc]	0.40 ± 0.05
n	< 1.2
Diffuse disc component	
$R_{e,F444W}$ [kpc]	1.72 ± 0.13
n	0.37 ± 0.08
Companion	
$R_{e,F444W}$ [kpc]	1.06 ± 0.13
n	0.61 ± 0.33
F277W	
Compact component	
$R_{e,F277W}$ [kpc]	0.58 ± 0.07
n	2.6 ± 0.8
Diffuse disc component	
Component not detected	
Companion	
$R_{e,F277W}$ [kpc]	1.7 ± 0.5
n	2.0 ± 1.4

Appendix B: FIR fitting

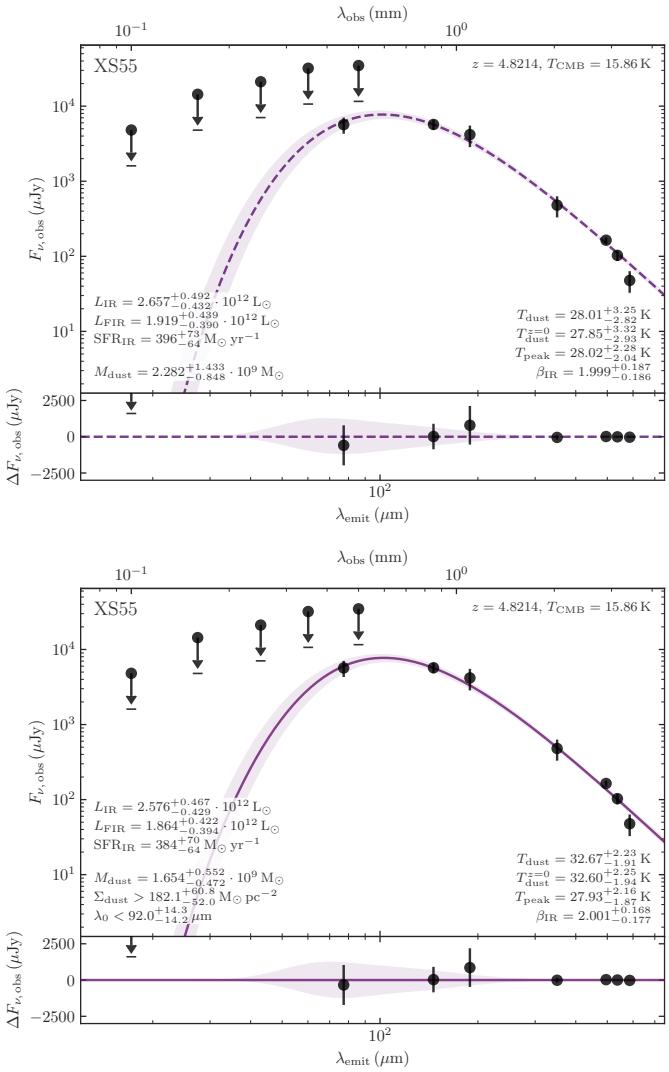

Fig. B.1. Mercurius FIR SEDs of XS55. **Left:** FIR-SED assuming optically thin dust. **Right:** FIR-SED assuming self-consistent optically thick dust, assuming an upper limit on the emission area of 9.08 kpc^2 (half-light radius of diffuse disc-like component in JWST/F444W).